CHEMISTRY OF MATERIALS

pubs.acs.org/cm

Article

Thermal Phase Control of Two-Dimensional Pt-Chalcogenide (Se and Te) Ultrathin Epitaxial Films and Nanocrystals

Jingfeng Li, Sadhu Kolekar, Yan Xin, Paula Mariel Coelho, Kinga Lasek, Florence A. Nugera, Humberto R. Gutiérrez, and Matthias Batzill*

Cite This: *Chem. Mater.* 2021, 33, 8018–8027

Read Online

ACCESS | Metrics & More | Article Recommendations

ABSTRACT: The controlled synthesis and modification of the composition of layered compounds are essential prerequisites for their deployment in electronic or chemical applications. Pt-chalcogenides exhibit various compositional phases. Here, we investigate how Pt-selenide and Pt-telluride phases can be obtained as ultrathin films or as supported nanocrystals by physical vapor deposition and thermal treatment. The films are characterized by scanning tunneling microscopy and spectroscopy, scanning transmission electron microscopy, and photoemission and Raman spectroscopy. In all cases, Pt-dichalcogenides are obtained by Pt and chalcogen codeposition at growth temperatures below 300 °C. These films can be grown by van der Waals epitaxy in a layer-by-layer fashion, enabling the characterization of the pronounced layer-dependent electronic properties of these compounds. Pt-telluride growth at elevated temperatures (above 400 °C) results in the formation of Pt-monotelluride. Interestingly, the thin film Pt-dichalcogenides can also be transformed into different phases with lower chalcogen concentration by post-growth vacuum annealing. Annealing-induced loss of chalcogen results in new composites. With this thermal process, an intermittent layered compound of Pt_3Te_4 is synthesized, which consists of alternating $PtTe_2$ and PtTe van der Waals layers. By thermal treatment of $PtSe_2$, we obtain a non-layered Pt-monoselenide in nanocrystalline form. PtSe is not reported in the bulk Pt-Se phase diagram, but its structure is analogue to the known Pt-monosulfide with a tetragonal unit cell. This PtSe phase is semiconducting with a band gap of ∼0.9 eV. The nanocrystalline PtSe phase is, however, unstable and easily loses more Se and eventually converts into Pt. Thus, it is demonstrated that post-growth thermally induced transformation of Pt-dichalcogenides films enables the synthesis of new Pt-chalcogenide phases as ultrathin films or nanocrystals.

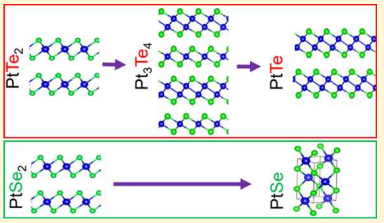

1. INTRODUCTION

Pt-chalcogenides exhibit interesting quantum properties that attracted attention both from a fundamental condensed matter physics perspective and for potential applications. $PtSe_2$ and $PtTe_2$ have been discussed for their topologically protected bulk electronic states,[1−6] which also suggested to have potentially important implications for spin orbit torque effects at magnetic interfaces.[7] In the ultrathin limits, these materials also showed strong layer dependence of their electronic structure with band gap openings as the materials are thinned to mono- or bilayer thickness.[8−14] This layer dependence of the electronic structure is attributed to strong interlayer interactions in these layered transition metal dichalcogenides that cause the semi-metallic to semiconductor transition as $PtSe_2$ or $PtTe_2$ is thinned to single layers. Surprisingly, $PtSe_2$ has been recently demonstrated to also exhibit magnetic properties.[15] These properties have been associated with native defects in the material that forms a diluted magnetic material, which may persist to the few to monolayer thick materials.[16] Potential practical uses of Pt-chalcogenides have been discussed[17,18] ranging from applications as electrodes for electrocatalysis,[19−23] pressure,[24] or gas sensors[25,26] to electronic[27−29] and opto-electronic applications.[17] Besides the mostly studied layered chalcogenides, other chalcogen-poor compositional phases may exist in the Pt-Se or Pt-Te phase diagrams.[30,31] Such phases have also been predicted to exhibit electrocatalytic properties,[32] but a controlled synthesis of Pt-chalcogenides with different compositions has not been well documented. It has, however, been shown that the CVD growth of Pt-telluride may result in PtTe or $PtTe_2$ depending on the growth conditions.[33] For Pt-selenide, it has been shown that exfoliated $PtSe_2$ can transition into a tetragonal PtSe phase by loss of Se.[34]

In this communication, we discuss the synthesis of Pt-Se (or Pt-Te) ultrathin films by physical vapor codeposition of Pt and chalcogens in ultrahigh vacuum, akin to molecular beam epitaxy, and to characterize the material's properties by

Received: June 22, 2021
Revised: October 4, 2021
Published: October 14, 2021

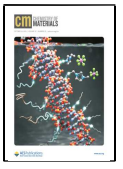

https://doi.org/10.1021/acs.chemmater.1c02163
Chem. Mater. 2021, 33, 8018−8027

scanning tunneling microscopy (STM) and X-ray photoemission spectroscopy (XPS). Here, the focus is on the approaches that enable us to obtain different compositional phases as ultrathin films and to characterize their basic properties.

2. RESULTS AND DISCUSSION

The high vapor pressure of chalcogens requires a high chalcogen-to-transition metal ratio for the growth of TMDs by codeposition on a substrate in vacuum. We employ a ratio of ~10:1 for the chalcogen:Pt ratio. However, even with such a high chalcogen over-supply, the film may not necessarily form with the highest chalcogen stoichiometry, *i.e.*, as dichalcogenides. While the growth temperature affects the chemical potential of the elements and their vapor pressure, vacuum growth processes of thin films are generally in non-thermodynamic equilibrium, which makes the prediction of resulting compositions based on thermodynamic arguments alone impossible. Thus, we explore experimentally the growth of Pt-telluride and Pt-selenide at different sample temperatures and find that the dichalcogenides are only obtained for low growth temperatures (~250−300 °C) while Pt-monotelluride may be obtained for growth at higher temperatures (400−450 °C). Also, the dichalcogenide ultrathin films can be transformed into chalcogen-deficient phases by post-growth vacuum annealing, suggesting the easy loss of chalcogen by desorption. The different phases obtained in this study are illustrated in Figure 1. The preparation conditions to obtain these phases are discussed separately for Pt-selenide and Pt-telluride.

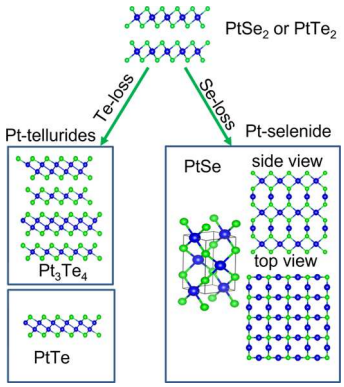

Figure 1. Schematic illustrations of Pt-telluride and selenide phases. While both chalcogenides form layered dichalcogenides, only the Pt-telluride exhibits tellurium-deficient layered compounds. A PtSe compound with a tetragonal unit cell, isostructural to PtS, is observed in this study.

2.1. Pt-Telluride. The core-level photoemission spectra for Pt-telluride and ex situ Raman spectroscopy for samples grown at low temperature (260 °C) and high temperature (400 °C) are shown in Figure 2a and Figure 2b, respectively. The Raman spectra show E_g and A_{1g} modes at 116 and 158 cm^{-1} that are representative for $PtTe_2$ for the low-temperature grown sample.[33] In contrast, the sample grown at high temperature exhibits two E_g and A_{1g} modes that are representative of PtTe, as schematically indicated in Figure 2b. The peaks at 92.1 and 185.1 cm^{-1} can be assigned to the E_g modes for PtTe, and peaks at 118.4 and 169.2 cm^{-1} correspond to the A_{1g} modes of PtTe.[33] Consequently, the sample grown at high temperature can be assigned to PtTe. The identification of the phases by Raman also allows us to assign the XPS peak positions to the two different materials. The Te-$3d_{5/2}$ peak shifts by 0.2 eV to lower binding energy for PtTe than for $PtTe_2$, and the Pt-$4f_{7/2}$ peak shifts from 72.9 eV for $PtTe_2$ to 72.0 eV for PtTe. The fact that both Pt and Te shift to lower binding energy for PtTe than for $PtTe_2$ suggests that the shift is not only a consequence of chemical (charge transfer) shifts but also that of other effects like a change in the Madelung energy contributing to the observed peak positions. The shift observed in the Pt peak may, however, have a contribution from a change in its charge state as it shifts to lower binding energy for PtTe than for $PtTe_2$, *i.e.*, closer to the peak position of elemental Pt at 71.1 eV. The different composition of the Pt-telluride prepared at low and high growth temperature is also apparent from the peak intensity ratio in XPS. The Te/Pt intensity ratio for the high-temperature grown sample is only 0.45 times that for the low-temperature grown sample, *i.e.*, the Te/Pt ratio for the low-temperature grown sample is close to twice that of the high-temperature grown sample consistent with $PtTe_2$ and PtTe. Peak positions and intensity ratios are summarized in Table 1.

Interestingly, starting with a $PtTe_2$ grown at low temperature and then subsequently annealing it in vacuum to 450 °C also cause a compositional transformation of the film. This can be observed for instance in XPS, as shown in Figure 2c. The Te-$3d_{5/2}$ peak position after annealing is similar to that for PtTe, but the Pt-4f peak is broadened compared to the pure PtTe and $PtTe_2$ film. In fact, the Pt-4f peak after annealing can be fitted with two components, each with the same line shape and full width at half-maximum (FWHM) as the peaks for PtTe and $PtTe_2$. One component is at the same position as the PtTe peak, and the other is only shifted slightly to lower binding energy than the peak of $PtTe_2$. The exact fitted peak positions are given in Table 1. This suggests that the two components originate from materials that are similar to $PtTe_2$ and PtTe. The intensity ratio of the two Pt-components is 4:7 or the $PtTe_2$:PtTe-like peaks. The Pt-Te phase diagram contains two intermediate phases between $PtTe_2$ and PtTe with compositions of Pt_2Te_3 and Pt_3Te_4.[35] These intermediate phases are also layered compounds and can be understood as alternating layers of $PtTe_2$ and PtTe. Pt_2Te_3 can be constructed of two layers of $PtTe_2$ alternating with one layer of PtTe (Pt_2Te_2) and Pt_3Te_4 by alternating $PtTe_2$ and PtTe (Pt_2Te_2) layers (see also Figure 1 for an illustration of Pt_3Te_4). Considering that the PtTe layer consists of two Pt layers sandwiched between Te layers, while $PtTe_2$ has only one Pt layer sandwiched between two Te layers (see Figure 1), the planar Pt atom density in a PtTe is twice that of $PtTe_2$ per layer. Thus, for Pt_2Te_3 (with two $PtTe_2$ layers alternating with one PtTe layer), the ratio of Pt atoms in a $PtTe_2$ or PtTe environment is 1:1, while for Pt_3Te_4 (one $PtTe_2$ layer alternating with one PtTe layer), the ratio is 1:2. From the fitting of the Pt-4f peak into $PtTe_2$ and PtTe components, we obtain a ratio of 4:7, which is only slightly off from the expected 1:2 ratio for Pt_3Te_4.

The Pt:Te peak intensity ratio also gives further evidence for a Pt_3Te_4 compound. We measure a Pt:Te intensity ratio of 0.26 (Table 1). This ratio is in between the ratios determined for $PtTe_2$ and PtTe films. Using the measured ratio of $PtTe_2$ as a calibration of the relative atomic sensitivity factors of our spectrometer, *i.e.*, multiplying the uncompensated XPS Pt:Te intensity ratios by a factor of 2.63 to obtain atomic Pt:Te ratios, we can estimate the actual atomic ratio of the annealed film to Pt:Te = 0.7, which is close to 3/4 and thus also

https://doi.org/10.1021/acs.chemmater.1c02163
Chem. Mater. 2021, 33, 8018−8027

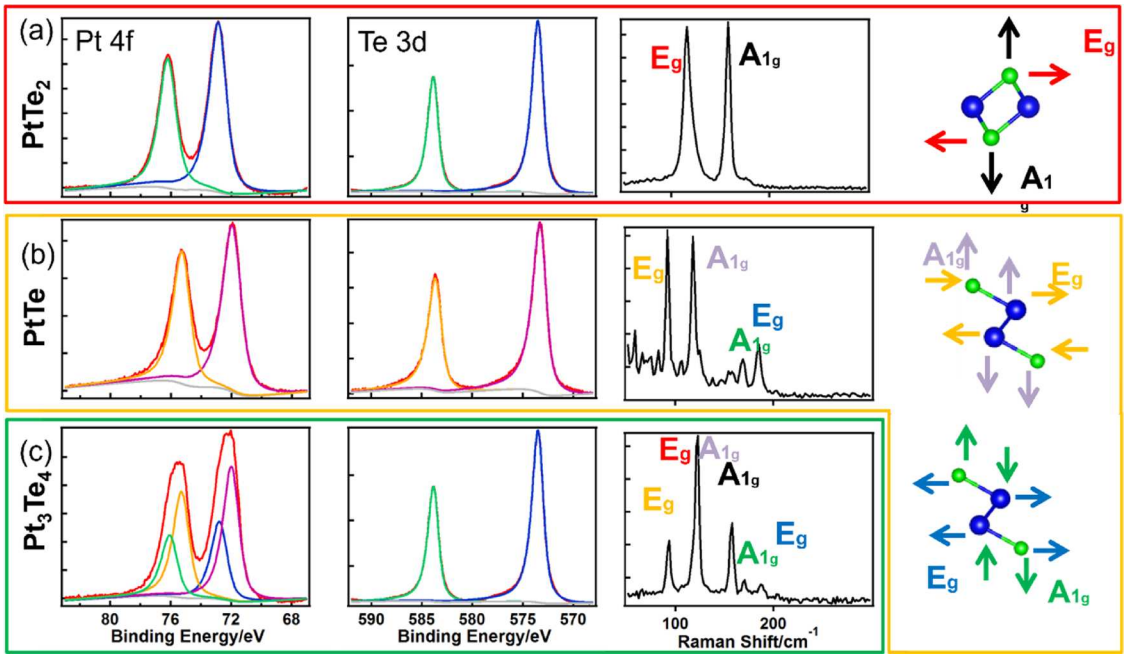

Figure 2. Spectroscopic characterization of Pt-telluride phases. XPS of Pt-4f and Te-3d core levels as well as Raman spectra are shown for (a) films grown at low temperatures (below 300 °C) and are assigned to $PtTe_2$, (b) films grown at 400 °C and are assigned to PtTe, and (c) films grown at below 300 °C and subsequently vacuum annealed to above 400 °C and are assigned to Pt_3Te_4.

Table 1. Summary of XPS and Raman for Pt-Telluride Phases

	XPS: Pt-$4f_{5/2}$/Pt-$4f_{7/2}$		XPS: Te-$3d_{1/2}$/Te-$3d_{3/2}$	XPS: intensity ratio Pt-4f/Se-3d (uncompensated)	Raman peak positions
$PtTe_2$	76.25/72.9 eV		583.9/573.4 eV	0.19	116 cm^{-1}
					158 cm^{-1}
PtTe	75.35/72.0 eV		583.7/573.2 eV	0.42	92.1 cm^{-1}
					118.4 cm^{-1}
					169.2 cm^{-1}
					185.1 cm^{-1}
Pt_3Te_4	component 1: 76.15/72. 8 eV	intensity ratio comp.1/comp.2 = 4/7	583.7/573.2 eV	0.26	94 cm^{-1}
					123.3 cm^{-1}
					158 cm^{-1}
	component 2:75.35/72.0 eV				118.4 cm^{-1}
					170.8 cm^{-1}
					187.2 cm^{-1}

consistent with a Pt_3Te_4 film. In a Pt_3Te_4 component consisting of alternating $PtTe_2$ and PtTe layers, charge transfer between the layers compared to pure $PtTe_2$ or PtTe is expected and this may explain the small shift of the $PtTe_2$ peak-component in the Pt-4f core level.

We also compare the Raman of the intermediate composition with those of PtTe and $PtTe_2$, as shown in Figure 2c. All peaks can be assigned to the E_g or A_{1g} peaks of either PtTe and/or $PtTe_2$ with only small but significant shifts of the peaks compared to the pure PtTe and $PtTe_2$ films (Table 1). This is further evidence that the film is structurally like a mixture of PtTe and $PtTe_2$.

Angle-resolved photoemission spectroscopy (ARPES) measurements for bilayer Pt-telluride films grown on single-crystal MoS_2 substrates before and after vacuum annealing are presented in Figure 3. Before annealing, we obtain spectra consistent with previous reports for $PtTe_2$ bilayers,[8,36] and after annealing and compositional conversion, an entirely new band structure is observed. This is confirmation that a new phase is formed, and all $PtTe_2$ is transformed since the electronic bands assigned to $PtTe_2$ do not remain as the direct comparison of the bands of the sample before and after annealing indicates. This suggests that the layered Pt_3Te_4 is thermodynamically favored over a phase separation into pure $PtTe_2$ and PtTe grains.

Further vacuum annealing, however, at higher temperatures causes further loss of tellurium, and eventually, a PtTe film forms. Thus, it appears that the PtTe films can be obtain by either direct high-temperature growth or by prolonged post-growth thermal annealing of a $PtTe_2$ film. On the other hand, the intermediate Pt_3Te_4 phase can be obtained in a controlled way by post-growth annealing of $PtTe_2$ and monitoring of the Pt-4f XPS peak ratios.

At the atomic scale, all Pt-tellurides exhibit a layered hexagonal structure with very similar lattice constants, which makes a distinction of the different phases by atomic-resolved STM challenging. On the larger scale, the different synthesis conditions result in different film morphologies. Growth at low temperatures enables us to obtain good layer growth. Very low temperatures (of 250 °C) are required to obtain monolayer

https://doi.org/10.1021/acs.chemmater.1c02163
Chem. Mater. 2021, 33, 8018−8027

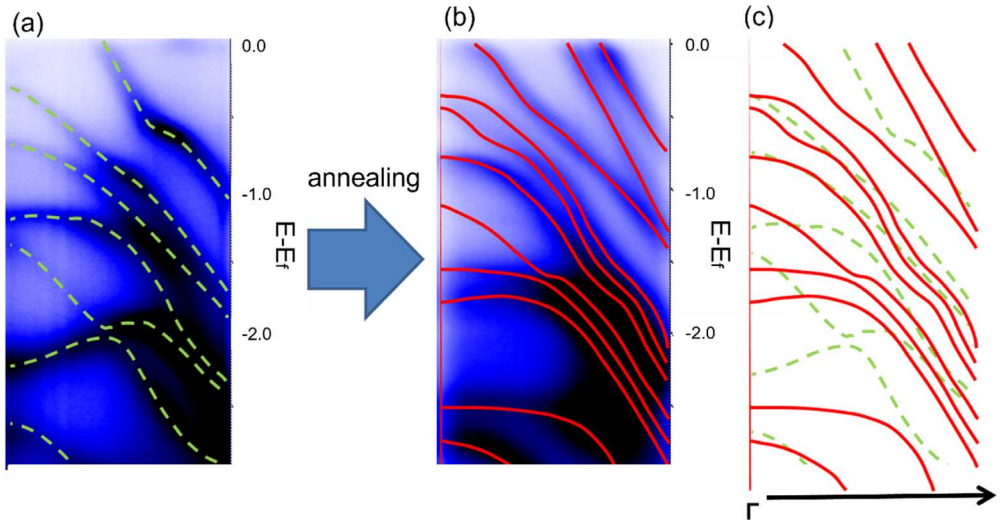

Figure 3. ARPES band structure of Pt-telluride. (a) Band structure of bilayer $PtTe_2$. The band structure after annealing of the same sample in vacuum is shown in panel (b). An overlay of the measured band structures is shown in panel (c) and indicates that annealing causes formation of a new phase.

$PtTe_2$, slight elevation of the growth temperature to above 300 °C always favors the growth of bilayer islands from the start, and monolayer films are not obtained. Also, the substrate plays a role in the surface morphology. Growth on graphite (HOPG) results in a rougher film than the growth on MoS_2 substrates. This difference may be a consequence of the stronger film−substrate interaction on MoS_2 than on graphite. Growth at 400 °C, which is required to obtain PtTe, results in rougher films than the low-temperature synthesis conditions of $PtTe_2$. Vacuum annealing of flat $PtTe_2$, which results in loss of Te and the transformation into Pt_3Te_4, does only cause a roughening for mono- to few-layer films that causes the formation of multilayer height islands rather than flat films. For initially multilayer $PtTe_2$ films, vacuum-annealed samples maintain a flat surface morphology even at an annealing temperature of 450 °C. The roughening of the very thin films may be a combination of a tendency of dewetting of the substrate and the requirement for the formation of thicker islands to accommodate the larger unit cell of Pt_3Te_4. Figure 4 shows film morphologies of Pt-telluride ultrathin films obtained for different synthesis conditions. The good layer growth at low growth temperatures and the possibility of its growth on single-crystal MoS_2 also enable the electronic structure characterization by ARPES of these films, as reported above. For the rougher PtTe films, we were not able to obtain ARPES data.

Cross-sectional scanning transmission electron microscopy (STEM) measurements were performed to identify the atomic structure for the above identified PtTe and Pt_3Te_4 samples. Figure 5a shows the PtTe phase on a MoS_2 substrate obtained by high-temperature post-growth annealing. Different structures for PtTe are possible according to crystal structure calculation databases for 2D materials.[37] The crystal structure observed in STEM is consistent with the *P*-3*m*1 space group, which is also the structure with the lowest formation energy according to ref 37 and was suggested by computation to be a potentially highly active oxygen reduction electrocatalyst.[32] Figure 5b shows the Pt_3Te_4 phase obtained by post-growth annealing of a $PtTe_2$ film. STEM confirms the alternating stacking of $PtTe_2$ and PtTe layers. Moreover, antiphase domains can be identified in which the stacking is reversed. This means that both $PtTe_2$ and PtTe surface terminations are possible.

A final check for the synthesis of Pt-dichalcogenides is to confirm the layer-dependent opening of a band gap. It has been predicted by density functional theory (DFT) simulations that monolayer $PtTe_2$ should be semiconducting with a band gap of ∼0.5 eV, while bilayer and multilayer samples are semimetallic, *i.e.*, the conduction and valence band overlap at the Fermi level.[11] The opening of a band gap for monolayer $PtTe_2$ has also been recently experimentally demonstrated in ARPES measurements.[8] We performed STS measurements on $PtTe_2$ islands grown on HOPG that exhibit monolayer, bilayer, and trilayer height terraces. The STS data, as shown in Figure 6a, indicate that the monolayer indeed exhibits a semiconducting band gap of 0.5 eV, while bi- and trilayer height islands are metallic, as also apparent from the ARPES data in Figure 3a. This is again consistent with the synthesis of $PtTe_2$. PtTe samples prepared by high-temperature growth are metallic as shown in the ultraviolet photoemission spectrum of a PtTe film, see Figure 6b. Pt_3Te_4 samples obtained by post-growth annealing of $PtTe_2$ are also metallic, as indicated by the ARPES spectra in Figure 3b.

Thus, our investigation of Pt-telluride shows that different compositional phases of Pt-telluride can be prepared by physical vapor deposition. $PtTe_2$ or PtTe can be obtained by controlling the growth temperature, while an intermediate Pt_3Te_4 phase can be accessed by vacuum annealing of $PtTe_2$. All these behaviors are linked to the presence of different layered Pt-telluride phases and the thermal desorption of tellurium. In the next section, we explore if the Pt-selenide system exhibits different equilibrium phases.

2.2. Pt-Selenide. Unlike Pt-telluride, the phase diagram of Pt-selenide contains only one layered compound, *i.e.*, $PtSe_2$. A Se-deficient Pt_5Se_4 phase is a 3D covalently bonded material, but DFT simulations suggested that it may also exist as a 2D monolayer material.[23] The $PtSe_2$ and Pt_5Se_4 are the only two line phases in the Pt-Se phase diagram for bulk compounds.[38] However, PtSe nanocrystals have been recently synthesized by vacuum annealing of $PtSe_2$.[34] This structure is also a 3D covalent bonded structure with a tetragonal unit cell and is isostructural to the known PtS structure.[39,40]

https://doi.org/10.1021/acs.chemmater.1c02163
Chem. Mater. 2021, 33, 8018−8027

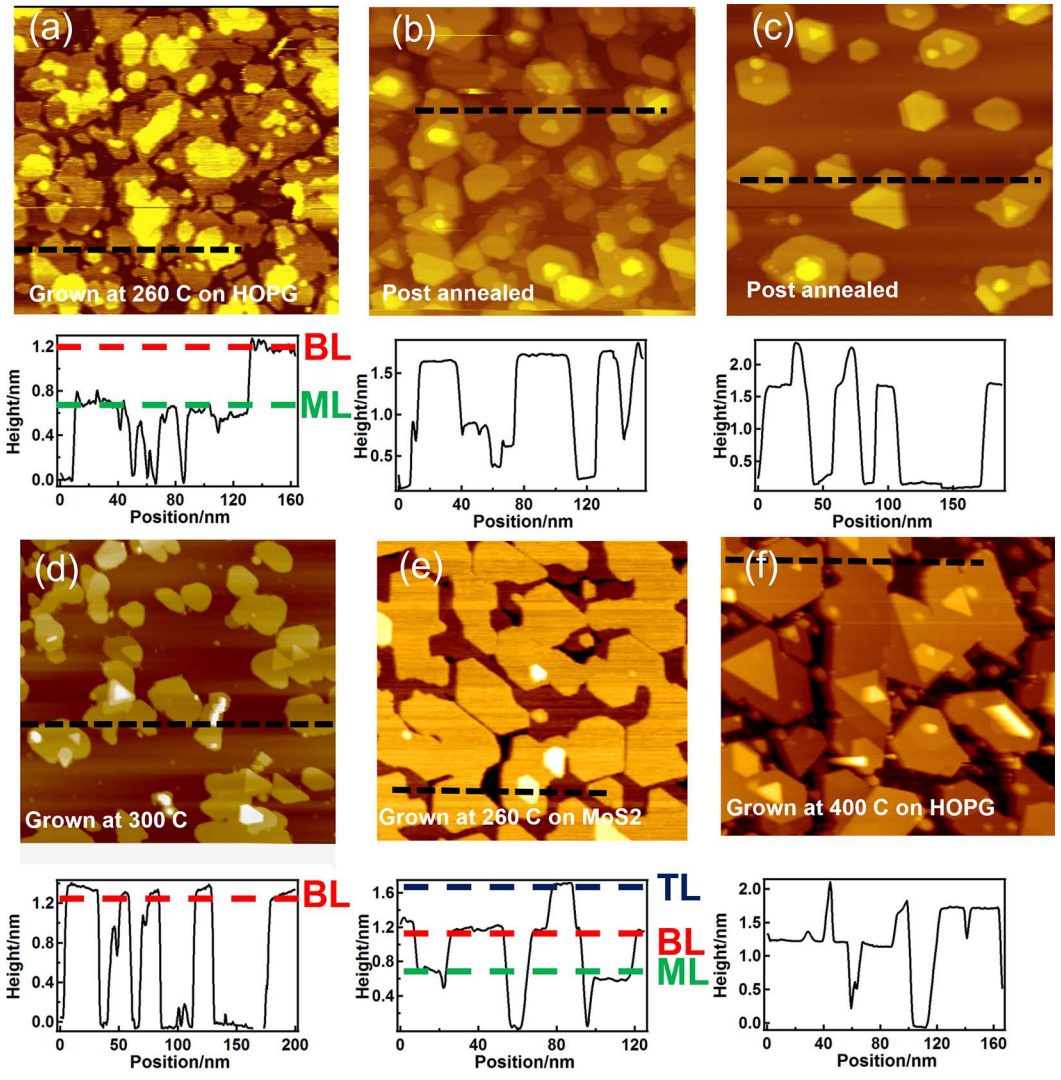

Figure 4. Film morphology characterization of Pt-telluride ultrathin films on HOPG and MoS_2. (a) $PtTe_2$ grown on HOPG at 260 °C. Both monolayer and bilayer islands are observed. (b) After annealing to 400 °C, monolayer regions disappear, and the film transforms into multilayer islands. After longer annealing shown in panel (c), islands become even larger and transform into Pt_3Te_4 (evidenced by XPS). Direct growth at 300 °C, shown in panel (d) on HOPG, also causes growth in an island mode, and no monolayers are observed. In contrast, growth on MoS_2 substrates under similar growth temperatures causes the formation of a much more uniform bilayer growth, as shown in panel (e). (f) Growth of multilayer PtTe on HOPG by growth at 400 °C results in large grains but no specific epitaxial orientation with the substrate as is evidenced from the random edge orientations of the islands. All images are 200 nm × 200 nm in size.

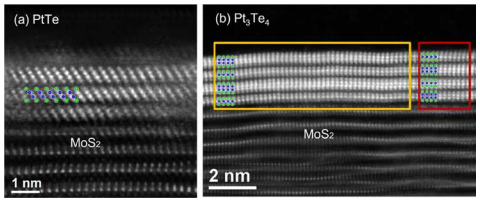

Figure 5. Scanning transmission electron micrographs of (a) PtTe and (b) Pt_3Te_4 ultrathin films on MoS_2 substrates. Panel (a) is taken along the [100] crystallographic direction, while panel (b) is taken along the [110] direction. The micrograph in panel (a) is consistent with PtTe with a *P*-3*m*1 space group structure. In panel (b), the alternating stacking of PtTe and $PtTe_2$ layers is observed. The yellow and red rectangles indicate two anti-phase domains with reversed stacking sequences.

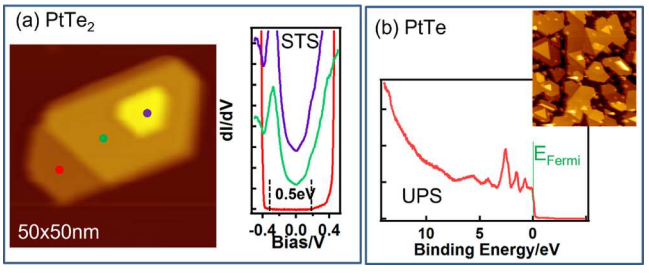

Figure 6. Electronic properties of Pt-tellurides. (a) STS measurements of the electronic band gap of a $PtTe_2$ island with different terrace heights. For the monolayer terraces, a band gap of 0.5 eV is measured (red), while bilayer (green) and trilayer (purple) height terraces exhibit a characteristic metallic V-shaped d*I*/d*V* spectrum. (b) UPS measurements on a PtTe multilayer film confirm its metallic properties. The inset shows the STM measurement of the film for which the UPS was collected.

Like for the Pt-telluride system, low-temperature growth results in the formation of dichalcogenides. This is confirmed

https://doi.org/10.1021/acs.chemmater.1c02163
Chem. Mater. 2021, 33, 8018−8027

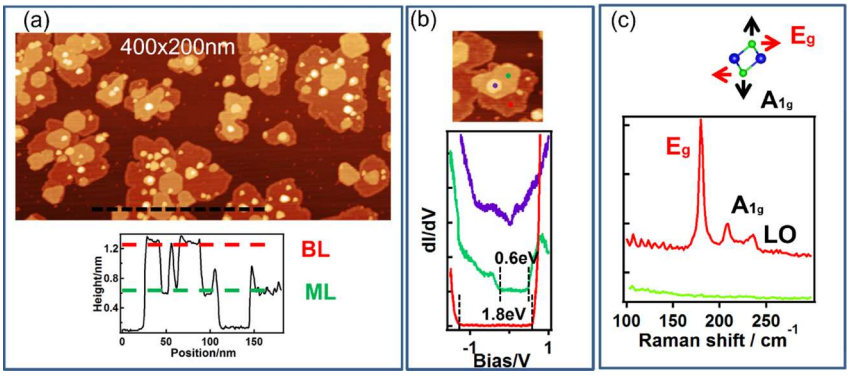

Figure 7. Characterization of $PtSe_2$. Submonolayer islands of $PtSe_2$ grown on HOPG are shown in panel (a). The line scan shows the height of the first two island terraces corresponding to the interlayer separation of $PtSe_2$. STS on mono-, bi-, and trilayer height terraces are shown in panel (b), illustrating the semiconducting to metal transition with increasing number of layers. Monolayer terraces have a band gap of 1.8 eV, bilayer islands have a band gap of 0.6 eV, and trilayer islands are metallic. The Raman spectrum shown in panel (c) confirms that the films are $PtSe_2$. The green line is the base line of the clean substrate.

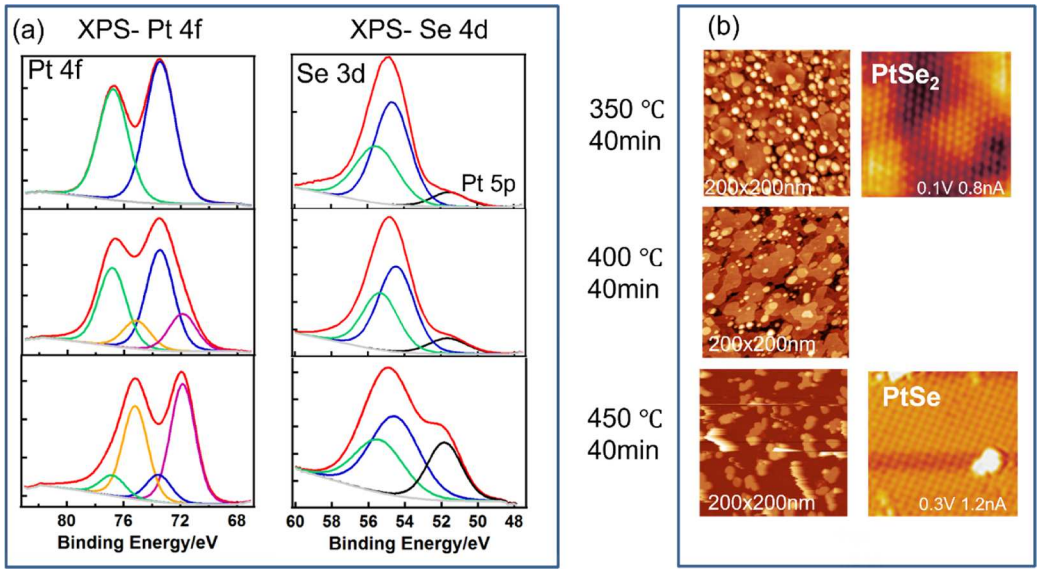

Figure 8. Compositional and morphological transformation of the Pt-selenide film by vacuum annealing. XPS data for Pt-4f and Se-3d is shown in panel (a) as the function of annealing temperature. The initial $PtSe_2$ film is gradually transformed into the PtSe film as evidenced by the loss of Se and the occurrence of the second Pt-4f component that gradually increases in intensity with increasing annealing. The compositional transformation is also associated with a strong morphology change of the film, as shown in the STM studies in panel (b). The initial flat $PtSe_2$ film increasingly roughens and forms taller islands. On the atomic scale, the hexagonal structure of $PtSe_2$ is transformed into a square surface unit cell, as shown in the atomic resolution STM images.

by STM and STS on nanoislands. The measured step height exhibits the expected interlayer separation, as shown in Figure 7a. Also, STS demonstrates the layer-dependent electronic properties expected for $PtSe_2$, with the monolayer exhibiting a semiconducting gap of 1.8 eV and bilayer islands with a gap of 0.6 eV, while multilayers are metallic, as shown in Figure 7b. Raman of the low-temperature grown sample, as shown in Figure 7c, is also consistent with that previously reported for $PtSe_2$.[33,41,42] XPS of $PtSe_2$ is shown in Figure 8, with the Pt-$4f_{5/2}$ and Pt-$4f_{7/2}$ peaks at 76.75/73.4 eV. The Se-$3d_{1/2}$ and Se-$3d_{3/2}$ are at 55.8/54.9 eV binding energy, respectively. The Pt-4f to Se-3d peak intensity ratio is measured to be 4.2:1 in our spectrometer. Raman and XPS peak positions and intensity ratios are summarized in Table 2.

Vacuum annealing of $PtSe_2$ films results again in the loss of Se, and a gradual transition is observed with formation of additional components in the Pt-4f and Se-3d peaks, see Figure 8a. With increasing annealing, the XPS peaks eventually convert entirely to the new peak position given in Table 2. The Pt-4f to Se-3d peak intensity ratio also changes to 9.1:1, which is only slightly more than the expected increase by a factor of 2 for a monoselenide compared to the intensity ratio for $PtSe_2$.

Table 2. Summary of XPS and Raman for Pt-Selenide

	XPS: Pt-$4f_{5/2}$/Pt-$4f_{7/2}$	XPS: Se-$3d_{1/2}$/Se-$3d_{3/2}$	XPS Pt-4f/Se-3d intensity ratio (uncompensated)	Raman peak positions
$PtSe_2$	76.75/73.40 eV	55.8/54.9 eV	4.2	179.9 cm^{-1}
				208.9 cm^{-1}
				236.1 cm^{-1}
PtSe	75.2/71.85 eV	55.8/54.9 eV	9.1	

https://doi.org/10.1021/acs.chemmater.1c02163
Chem. Mater. 2021, 33, 8018−8027

STM measurements also show that the compositional transformation is accompanied in a morphological change of the film, see Figure 8b. The initial flat $PtSe_2$ films are transformed in taller grains and a dewetting of the substrate. These taller grains exhibit a square atomic corrugation in contrast to the hexagonal structure of $PtSe_2$. With increasing annealing, the taller islands associated with PtSe grow in size. The gradual transformation observed in XPS and the gradual change in island morphology suggest that the compositional transformation of $PtSe_2$ into PtSe is a nucleation growth process rather than the $PtSe_2$ phase uniformly loosing Se. The square surface structure observed in STM is consistent with a PtS-like PtSe phase, as shown in Figure 9, rather than the known Pt_5Se_4 bulk phase. Figure 9a shows Raman spectroscopy of the pure $PtSe_2$ phase and of a mixed $PtSe_2$/PtSe phase after vacuum annealing as is apparent from the large-scale STM image that allows us to identify both phases. The PtSe nanocrystals are fairly thin with typical heights in STM of 2−2.5 nm and a lateral extension of 10−20 nm. In Raman, the transformation causes the appearance of new peaks in a broad range from 350 to 450 cm^{-1}, and this is the same range where Raman peaks for the isostructural PtS phase are observed.[40] STM studies of a mixed region shown in Figure 9b enable the measurement of the surface lattice constant of the square PtSe phase by using the known lattice constant of the hexagonal $PtSe_2$ phase as a reference. From the line scans shown in Figure 9b, we determine the lattice constant of the square surface unit cell of PtSe to 0.357 nm. The similarity in the lattice constant of PtSe with that of $PtSe_2$ may assist in the stabilization of the PtSe phase at the interface to $PtSe_2$. Importantly, the surface measurements conducted here by STM are in perfect agreement to the previously reported *in situ* STEM observation of this phase change.[34] For instance, in Figure 4 in ref 34, a similar $PtSe_2$/PtSe interface is observed to the one shown here by STM in Figure 9b. The PtSe structure determined by STEM is shown in Figure 9c in the side and top view. In STM, we only image the very top-most atoms and thus we may only observe the square lattice indicated by the red square in the top view. The overlay of the structure with an STM image is also shown in Figure 9c. Thus, our STM measurements confirm the formation of the previously reported thermal transformation of thin $PtSe_2$ into nanocrystals with a PtS structure. The transformation into PtSe rather than the known Pt_5Se_4 phase may be a consequence of the lower surface energy for the PtS structure that then stabilizes this structure for the nanocrystals with their high surface-to-volume ratio.

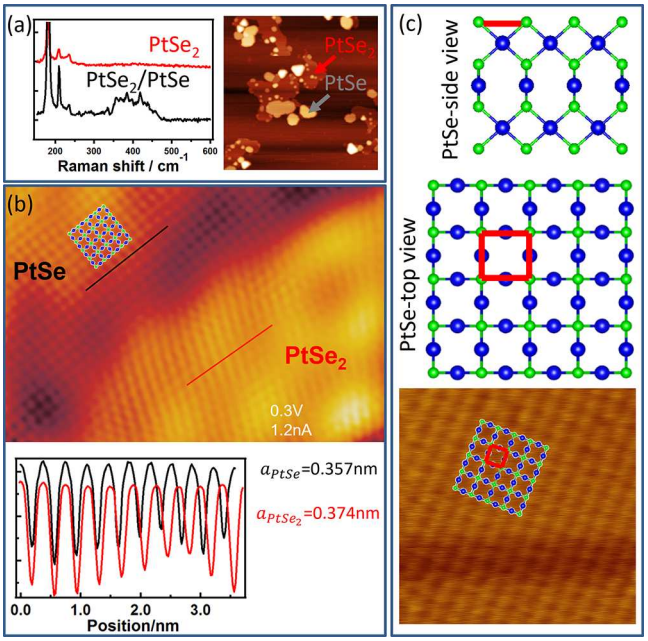

Figure 9. Characterization of the PtSe phase. (a) Raman of pure $PtSe_2$ (red) and after partial transformation into PtSe by thermal annealing (black). The larger-scale STM image shows the presence of both $PtSe_2$ and PtSe nanocrystals. An interface region between PtSe and $PtSe_2$ is shown in panel (b). The corresponding line profiles enable the measurement of the lattice constant of the square surface unit cell of the PtSe phase to 0.357 nm, which is referenced to the known unit cell of $PtSe_2$. (c) Illustration of the tetragonal unit cell of PtSe (isostructural to PtS) as a side view and top view. The square top view structure is overlayed with the STM image.

Post-growth annealing of a $PtSe_2$ film is required to synthesize this new PtSe nanocrystalline phase. This synthesis approach will enable us to characterize the chemical and physical properties of this material further. Since the isostructural PtS is a semiconductor,[40] one main question is if PtSe also exhibits a band gap. We performed STS measurements on a mixed island that exhibits both PtSe and $PtSe_2$ regions as determined from the atomic resolution images that are easily distinguished between the square and hexagonal surface unit cells. STS data across the contact line of these two phases show that, as expected, $PtSe_2$ is metallic, but the PtSe region shows a pronounced band gap of ∼0.9 eV, see Figure 10. The gap is almost unaltered to within 1.5 nm from the interface to the metallic $PtSe_2$. Only very close to the interface (less than 1 nm away), the gap narrows a bit and there are indications of metallic states from the $PtSe_2$ to spill into the band gap. Importantly, there is no indication of the band edges of PtSe to shift close to the interface, suggesting that the heterophase contact is an ohmic flat-band contact. PtSe is a

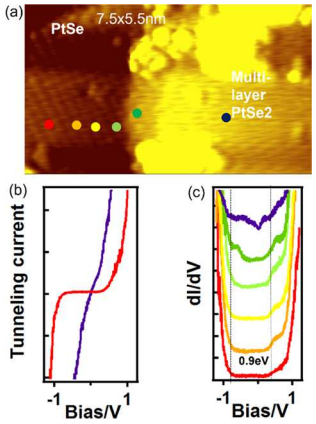

Figure 10. Electronic structure characterization of a PtSe/$PtSe_2$ junction by STS. (a) STM image of a PtSe/$PtSe_2$ grain boundary region. Points at which STS spectra were collected are indicated by the colored points. The $PtSe_2$ multilayer grain is metallic, while the PtSe grain is semiconducting with a band gap of 0.9 eV. The contrast between metallic and semiconducting regions is apparent in the $I-V$ curves (b) as well as in the dI/dV spectra (c). The valence band maximum and conduction band minimum for PtSe are indicated by the dashed lines in panel (c). No shift of the band edges as a function of distance from the grain boundary is observed, suggesting an ohmic heterojunction.

https://doi.org/10.1021/acs.chemmater.1c02163
Chem. Mater. 2021, 33, 8018−8027

new semiconducting material, which expands the toolbox of the Pt-chalcogenides. Opportunities to convert $PtSe_2$ locally into PtSe by, e.g., laser heating, can be potentially used for making planar metal-semiconducting junctions. Similar phase change-induced contacts have been proposed for other layered materials.[43] Among all the selenides and tellurides synthesized, here, PtSe is the only semiconducting material.

3. CONCLUSIONS

The controlled synthesis of Pt-selenides and Pt-tellurides in different compositional phases has been studied for ultrathin films grown by physical vapor codeposition of Pt and chalcogens. The selenides and tellurides have in common that the dichalcogenides are only obtained for low growth temperatures below 300 °C. Growth at high growth temperatures (∼400 °C) favors the formation of Pt-monotelluride, while we were not able to synthesize PtSe by a direct growth. Interestingly, different phases are obtained by post-growth transformation of the Pt-dichalcogenides by vacuum annealing compared to the phases obtained by high-temperature growth. Vacuum annealing induces a loss of chalcogens and thus a transformation of the dichalcogenides to phases with a lower chalcogen content. For Pt-telluride, we were able to obtain an intermediate Pt_3Te_4 phase that consists of alternating PtTe and $PtTe_2$ layers. Once the Pt_3Te_4 phase has formed, it is stable and only prolonged annealing allows us to transform it further into PtTe. Eventually, the film decomposes completely into metallic Pt at elevated temperatures. We speculate that the intermediate phase of Pt_3Te_4 is difficult to grow directly because it consists of alternating PtTe and $PtTe_2$ layers, and by tuning the growth temperature, either the one or the other pure phases is favored. Thermodynamically, though, Pt_3Te_4 has a formation energy that is below the connecting line between $PtTe_2$ and PtTe in a composition vs energy diagram[44] and thus forms preferably if multilayers of $PtTe_2$ lose Te.

For Pt-selenide, $PtSe_2$ is the only stable layered compound in the Pt-Se phase diagram. The other known bulk phase in the Pt-Se phase diagram is Pt_5Se_4; however, this phase is not obtained in this study. Similar to $PtTe_2$, $PtSe_2$ also loses chalcogens during vacuum annealing and this causes a transformation into a selenium poor phase. The phase we obtain is Pt-monoselenide as a new phase that is isostructural to PtS with a tetragonal unit cell. Thus, it appears that this new phase is formed either due to surface stabilization effects for nanoclusters or is a consequence of kinetic effects in the transformation process from $PtSe_2$ to PtSe. Our STS measurements indicate that this new tetragonal phase of PtSe is a semiconductor with a band gap of ∼0.9 eV. This is the only semiconducting phase of the Pt-selenide or telluride phases studied here, apart from the ultrathin Pt-dichalcogenides that also open a band gap in the monolayer limit.

Given the interest of Pt-chalcogenides as potential electrodes for electrochemical applications or as gas and pressure sensors, the synthesis of controlled phases is crucial. Physical vapor deposition can be an important approach for the synthesis of ultrathin films and nanostructured materials. Our findings indicate, however, that different phases can be obtained by post-growth annealing-induced chalcogen desorption compared to direct growth methods. Thus, post-growth annealing is a valuable approach for the synthesis of new chalcogen-containing materials with potential useful properties for chemical transformation reactions that should be further studied in future experiments.

4. EXPERIMENTAL SECTION

The syntheses of selenides and tellurides were conducted in two separate, dedicated UHV growth chambers. In both systems, Pt was evaporated from a 2 mm Pt wire in a water-cooled mini-e beam evaporator. Se or Te was supplied by evaporation from a water-cooled crucible. As a growth substrate, van der Waals materials were used to ensure the formation of van der Waals interfaces between the Pt-chalcogenides and the substrate. Either HOPG or MoS_2 crystals was used. The crystals were freshly cleaved in air and immediately introduced into the vacuum chamber. Before film deposition, the crystals were outgassed at 400 °C for 12 h in the growth chamber.

The growth morphology and atomic structure were studied by UHV-STM. Three different STMs have been used. The telluride growth chamber was connected via a vacuum transfer to a variable temperature STM operated at RT, and the selenide growth chamber was connected to a surface analysis chamber equipped for photoemission and room-temperature STM. In addition, a closed cycle He-cooled STM has been used for additional imaging and scanning tunneling spectroscopy investigations of the electronic structure have been used. Samples could be transferred with a vacuum suitcase from the growth chambers or directly through air as the Pt-dichalcogenides are stable in air. All STMs used electrochemically etched tungsten tips that were cleaned in-vacuum by voltage pulsing.

X-ray photoemission (XPS) was performed with non-monochromatized Al-K_α radiation from a dual-anode X-ray source. Two different XPS analyzers were used for selenides and tellurides, located in two different analysis UHV chambers connected to the selenide and telluride MBE growth chambers. A Scienta R3000 electron analyzer was used for detecting the photoemitted electrons for the Pt-telluride samples, while an Omicron Sphera electron analyzer was used for Pt-selenide samples. All binding energies were calibrated to the C-1s peak of the HOPG substrate, with the carbon peak set to a binding energy of 284.8 eV. In addition to XPS, we also collected the angle-resolved photoemission (ARPES) spectra for Pt-telluride samples grown on MoS_2 substrates. For ARPES, the same electron analyzer was used and a refocused UV-He discharge lamp was used to generate He-I radiation.

STEM studies were conducted at the High Magnetic Field Laboratory in Tallahassee, Florida. A focus ion beam (FIB) was used to cut a thin lamella into the samples for cross-sectional analysis with a 200 keV electron beam. STEM imaging was carried out in an aberration-corrected JEOL JEM-ARM200cF with a cold-field emission gun at 200 kV. The STEM resolution of the microscope was 0.78 Å. The STEM images were collected with a JEOL high-angle annular dark-field (HAADF) detector using the following experimental conditions: a probe of size 7c, CL aperture of 30 μm, scan speed of 32 μs/pixel, and camera length of 8 cm, which correspond to a probe convergence angle of 21 mrad and inner collection angle of 76 mrad.

Room-temperature Raman spectra were collected ex situ on these air stable samples using a 532 nm diode laser as the excitation wavelength in a Horiba LabRAM HR Evolution Raman system. The spectra were taken for areas of 20 × 20 μm^2 using the fast laser scanning mode (DuoScan) that minimizes sample heating and damage and provides an averaged spectrum of the sample. Laser powers of 0.19 and 0.89 mW were used for the platinum tellurides and selenides, respectively. The Raman was collected in back-scattering geometry through a 100× objective and detected by a Synapse back-illuminated deep deletion CCD (1024 × 256 pixels).

AUTHOR INFORMATION

Corresponding Author

Matthias Batzill − *Department of Physics, University of South Florida, Tampa, Florida 33620, United States;* orcid.org/0000-0001-8984-8427; Email: mbatzill@usf.edu

Authors

Jingfeng Li − *Department of Physics, University of South Florida, Tampa, Florida 33620, United States*

https://doi.org/10.1021/acs.chemmater.1c02163
Chem. Mater. 2021, 33, 8018−8027

Sadhu Kolekar − *Department of Physics, University of South Florida, Tampa, Florida 33620, United States*
Yan Xin − *National High Magnetic Field Laboratory, Florida State University, Tallahassee, Florida 32310, United States*
Paula Mariel Coelho − *Department of Physics, University of South Florida, Tampa, Florida 33620, United States*
Kinga Lasek − *Department of Physics, University of South Florida, Tampa, Florida 33620, United States*
Florence A. Nugera − *Department of Physics, University of South Florida, Tampa, Florida 33620, United States*
Humberto R. Gutiérrez − *Department of Physics, University of South Florida, Tampa, Florida 33620, United States;* orcid.org/0000-0001-8997-5274

Complete contact information is available at: https://pubs.acs.org/10.1021/acs.chemmater.1c02163

Author Contributions

J.L., S.K., P.M.C., and K.L. synthesized the samples and characterized them by photoemission and scanning tunneling microscopy. Y.X. conducted STEM measurements. F.A.N. and H.R.G. performed Raman characterization. M.B. directed the research and wrote the paper with contributions from all the authors.

Notes

The authors declare no competing financial interest.

■ ACKNOWLEDGMENTS

Financial support from NSF under awards 2140038 and 1701390 is acknowledged. TEM work was performed at the National High Magnetic Field Laboratory, which is supported by the National Science Foundation Cooperative Agreement no. DMR-1644779 and the State of Florida.

■ REFERENCES

(1) Bahramy, M. S.; Clark, O. J.; Yang, B.-J.; Feng, J.; Bawden, L.; Riley, J. M.; Marković, I.; Mazzola, F.; Sunko, V.; Biswas, D.; Cooil, S. P.; Jorge, M.; Wells, J. W.; Leandersson, M.; Balasubramanian, T.; Fujii, J.; Vobornik, I.; Rault, J. E.; Kim, T. K.; Hoesch, M.; Okawa, K.; Asakawa, M.; Sasagawa, T.; Eknapakul, T.; Meevasana, W.; King, P. D. C. Ubiquitous Formation of Bulk Dirac Cones and Topological Surface States from a Single Orbital Manifold in Transition-Metal Dichalcogenides. *Nat. Mater.* **2017**, *17*, 21−28.
(2) Pi, L.; Li, L.; Liu, K.; Zhang, Q.; Li, H.; Zhai, T. Recent Progress on 2D Noble-Transition-Metal Dichalcogenides. *Adv. Funct. Mater.* **2019**, *29*, 1904932.
(3) Yan, M.; Huang, H.; Zhang, K.; Wang, E.; Yao, W.; Deng, K.; Wan, G.; Zhang, H.; Arita, M.; Yang, H.; Sun, Z.; Yao, H.; Wu, Y.; Fan, S.; Duan, W.; Zhou, S. Lorentz-Violating Type-II Dirac Fermions in Transition Metal Dichalcogenide $PtTe_2$. *Nat. Commun.* **2017**, *8*, 257.
(4) Huang, H.; Zhou, S.; Duan, W. Type-II Dirac Fermions in the $PtSe_2$ Class of Transition Metal Dichalcogenides. *Phys. Rev. B* **2016**, *94*, 121117.
(5) Zhang, K.; Yan, M.; Zhang, H.; Huang, H.; Arita, M.; Sun, Z.; Duan, W.; Wu, Y.; Zhou, S. Experimental Evidence for type-II Dirac Semimetal in $PtSe_2$. *Phys. Rev. B* **2017**, *96*, 125102.
(6) Yang, H.; Schmidt, M.; Süss, V.; Chan, M.; Balakirev, F. F.; McDonald, R. D.; Parkin, S. S. P.; Felser, C.; Yan, B.; Mol, P. J. W. Quantum Oscillations in the type-II Dirac Semi-Metal Candidate $PtSe_2$. *New J. Phys.* **2018**, *20*, No. 043008.
(7) Xu, H.; Wei, J.; Zhou, H.; Feng, J.; Xu, T.; Du, H.; He, C.; Huang, Y.; Zhang, J.; Liu, Y.; Wu, H.-C.; Guo, C.; Wang, X.; Guang, Y.; Wei, H.; Peng, Y.; Jiang, W.; Yu, G.; Han, X. High Spin Hall Conductivity in Large-Area Type-II Dirac Semimetal $PtTe_2$. *Adv. Mater.* **2020**, *32*, 2000513.
(8) Li, J.; Kolekar, S.; Ghorbani-Asl, M.; Lehnert, T.; Biskupek, J.; Kaiser, U.; Krasheninnikov, A. V.; Batzill, M. Layer-Dependent Band Gaps of Platinum Dichalcogenides. *ACS Nano* **2021**, *15*, 13249−13259.
(9) Lin, M.-K.; Villaos, R. A. B.; Hlevyack, J. A.; Chen, P.; Liu, R.-Y.; Hsu, C.-H.; Avila, J.; Mo, S.-K.; Chuang, F.-C.; Chiang, T.-C. Dimensionality-Mediated Semimetal-Semiconductor Transition in Ultrathin $PtTe_2$ Films. *Phys. Rev. Lett.* **2020**, *124*, No. 036402.
(10) Wang, Y.; Li, L.; Yao, W.; Song, S.; Sun, J. T.; Pan, J.; Ren, X.; Li, C.; Okunishi, E.; Wang, Y.-Q.; Wang, E.; Shao, Y.; Zhang, Y. Y.; Yang, H.-T.; Schwier, E. F.; Iwasawa, H.; Shimada, K.; Taniguchi, M.; Cheng, Z.; Zhou, S.; Du, S.; Pennycook, S. J.; Pantelides, S. T.; Gao, H.-J. Monolayer $PtSe_2$, a New Semiconducting Transition-Metal Dichalcogenide, Epitaxially Grown by Direct Selenization of Pt. *Nano Lett.* **2015**, *15*, 4013−4018.
(11) Villaos, R. A. B.; Crisostomo, C. P.; Huang, Z.-Q.; Huang, S.-M.; Padama, A. A. B.; Albao, M. A.; Lin, H.; Chuang, F.-C. Thickness Dependent Electronic Properties of Pt Dichalcogenides. *npj 2D Mater. Appl.* **2019**, *3*, 2.
(12) Ciarrocchi, A.; Avsar, A.; Ovchinnikov, D.; Kis, A. Thickness-Modulated Metal-to-Semiconductor Transformation in a Transition Metal Dichalcogenide. *Nat. Commun.* **2018**, *9*, 919.
(13) Shi, J.; Huan, Y.; Hong, M.; Xu, R.; Yang, P.; Zhang, Z.; Zou, X.; Zhang, Y. Chemical Vapor Deposition Grown Large Scale Atomically Thin Platinum Diselenide with Semimetal−Semiconductor Transition. *ACS Nano* **2019**, *13*, 8442−8451.
(14) Lasek, K.; Li, J.; Kolekar, S.; Coelho, P. M.; Guo, L.; Zhang, M.; Wang, Z.; Batzill, M. Synthesis and Characterization of 2D Transition Metal Dichalcogenides: Recent Progress from a Vacuum Surface Science Perspective. *Surf. Sci. Rep.* **2021**, *76*, 100523.
(15) Avsar, A.; Ciarrocchi, A.; Pizzochero, M.; Unuchek, D.; Yazyev, O. V.; Kis, A. Defect Induced, Layer-Modulated Magnetism in Ultrathin Metallic $PtSe_2$. *Nat. Nanotechnol.* **2019**, *14*, 674−678.
(16) Avsar, A.; Cheon, C.-Y.; Pizzochero, M.; Tripathi, M.; Ciarrocchi, A.; Yazyev, O. V.; Kis, A. Probing Magnetism in Atomically Thin Semiconducting $PtSe_2$. *Nat. Commun.* **2020**, *11*, 4806.
(17) Wang, G.; Wang, Z.; McEvoy, N.; Fan, P.; Blau, W. J. Layered $PtSe_2$ for Sensing, Photonic, and (Opto-) Electronic Applications. *Adv. Mater.* **2021**, *33*, 2004070.
(18) Chen, E.; Xu, W.; Chen, J.; Warner, J. H. 2D Layered Noble Metal Dichalcogenides (Pt, Pd, Se, S) for Electronics and Energy Applications. *Mater. Today Adv.* **2020**, *7*, 100076.
(19) Chia, X.; Adriano, A.; Lazar, P.; Sofer, Z.; Luxa, J.; Pumera, M. Layered Platinum Dichalcogenides (PtS_2, $PtSe_2$, and $PtTe_2$) Electrocatalysis: Monotonic Dependence on the Chalcogen Size. *Adv. Funct. Mater.* **2016**, *26*, 4306−4318.
(20) Rosli, N. F.; Mayorga-Martinez, C. C.; Latiff, N. M.; Rohaizad, N.; Sofer, Z.; Fisher, A. C.; Pumera, M. Layered $PtTe_2$ Matches Electrocatalytic Performance of Pt/C for Oxygen Reduction Reaction with Significantly Lower Toxicity. *ACS Sustainable Chem. Eng.* **2018**, *6*, 7432−7441.
(21) Huang, H.; Fan, X.; Singh, D. J.; Zheng, W. Modulation of Hydrogen Evolution Catalytic Activity of Basal Plane in Monolayer Platinum and Palladium Dichalcogenides. *ACS Omega* **2018**, *3*, 10058−10065.
(22) Lina, S.; Liua, Y.; Hub, Z.; Luc, W.; Maka, C. H.; Zenga, L.; Zhaoa, J.; Lia, Y.; Yana, F.; Tsanga, Y. H.; Zhanga, X.; Lau, S. P. Tunable Active Edge Sites in $PtSe_2$ Films Towards Hydrogen Evolution Reaction. *Nano Energy* **2017**, *42*, 26−33.
(23) Yuan, J. H.; Li, L. H.; Zhang, W.; Xue, K.-H.; Wang, C.; Wang, J.; Miao, X. S.; Zeng, X. C. Pt_5Se_4 Monolayer: A Highly Efficient Electrocatalyst toward Hydrogen and Oxygen Electrode Reactions. *ACS Appl. Mater. Interfaces* **2020**, *12*, 13896−13903.
(24) Wagner, S.; Yim, C.; McEvoy, N.; Kataria, S.; Yokaribas, V.; Kuc, A.; Pindl, S.; Fritzen, C.-P.; Heine, T.; Duesberg, G. S.; Lemme, M. C. Highly Sensitive Electromechanical Piezoresistive Pressure Sensors Based on Large-Area Layered $PtSe_2$ Films. *Nano Lett.* **2018**, *18*, 3738.

(25) Sajjad, M.; Montes, E.; Singh, N.; Schwingenschlögl, U. Superior Gas Sensing Properties of Monolayer $PtSe_2$. *Adv. Mater. Interfaces* **2017**, *4*, 1600911.
(26) Yim, C.; Lee, K.; McEvoy, N.; O'Brien, M.; Riazimehr, S.; Berner, N. C.; Cullen, C. P.; Kotakoski, J.; Meyer, J. C.; Lemme, M. C.; Duesberg, G. S. High-Performance Hybrid Electronic Devices from Layered $PtSe_2$ Films Grown at Low Temperature. *ACS Nano* **2016**, *10*, 9550−9558.
(27) Wang, Z.; Li, Q.; Besenbacher, F.; Dong, M. Facile Synthesis of Single Crystal $PtSe_2$ Nanosheets for Nanoscale Electronics. *Adv. Mater.* **2016**, *28*, 10224−10229.
(28) Zhao, Y.; Qiao, J.; Yu, Z.; Yu, P.; Xu, K.; Lau, S. P.; Zhou, W.; Liu, Z.; Wang, X.; Ji, W.; Chai, Y. High-Electron-Mobility and Air-Stable 2D Layered $PtSe_2$ FETs. *Adv. Mater.* **2017**, *29*, 1604230.
(29) Das, T.; Yang, E.; Seo, J. E.; Kim, J. H.; Park, E.; Kim, M.; Seo, D.; Kwak, J. Y.; Chang, J. Doping-Free All $PtSe_2$ Transistor via Thickness-Modulated Phase Transition. *ACS Appl. Mater. Interfaces* **2021**, *13*, 1861−1871.
(30) Guo, C.; Huang, L.; Li, C.; Shang, S.; Du, Z. Thermodynamic Modeling of the Pt-Te and Pt-Sb-Te Systems. *J. Electr. Mater.* **2015**, *44*, 2638−2650.
(31) Kim, W.-S. Re-Investigation of the Phase Constitution of the System Pt-Te. *Metals Mater.* **1996**, *2*, 9.
(32) Wang, Y.; Li, Y.; Heine, T. PtTe Monolayer: Two-Dimensional Electrocatalyst with High Basal Plane Activity toward Oxygen Reduction Reaction. *J. Am. Chem. Soc.* **2018**, *140*, 12732−12735.
(33) Zhang, K.; Wang, M.; Zhou, X.; Wang, Y.; Shen, S.; Deng, K.; Peng, H.; Li, J.; Lai, X.; Zhang, L.; Wu, Y.; Duan, W.; Yu, P.; Zhou, S. Growth of Large Scale PtTe, $PtTe_2$ and $PtSe_2$ Films on a Wide Range of Substrates. *Nano Res.* **2021**, *14*, 1663−1667.
(34) Ryu, G. H.; Chen, J.; Wen, Y.; Warner, J. H. In-Situ Atomic-Scale Dynamics of Thermally Driven Phase Transition of 2D Few-Layered 1T $PtSe_2$ into Ultrathin 2D Nonlayered PtSe Crystals. *Chem. Mater.* **2019**, *31*, 9895−9903.
(35) Cenzual, K.; Gelato, L. M.; Penzo, M.; Parthé, E. Overlooked Triagonal Symmetry in Structures Reported with Monoclinic Centered Bravais Lattices, Trigonal Description of Li_8Pb_3, PtTe, Pt_3Te_4, Pt_2Te_3, $LiFe_6Ge_4$, $LiFe_6Ge_5$, $CaGa_6Te_{10}$, and $La_{3.266}Mn_{1.1}S_6$. *Z. Kristallogr. - Cryst. Mater.* **1990**, *193*, 217−242.
(36) Deng, K.; Yan, M.; Yu, C.-P.; Li, J.; Zhou, X.; Zhang, K.; Zhao, Y.; Miyamoto, K.; Okuda, T.; Duan, W.; Wu, Y.; Zhong, X.; Zhou, S. Crossover from 2D Metal to 3D Dirac Semimetal in Metallic $PtTe_2$ Films with Local Rashba Effect. *Sci. Bull.* **2019**, *64*, 1044−1048.
(37) Haastrup, S.; Strange, M.; Pandey, M.; Deilmann, T.; Schmidt, P. S.; Hinsche, N. F.; Gjerding, M. N.; Torelli, D.; Larsen, P. M.; Riis-Jensen, A. C.; Gath, J.; Jacobsen, K. W.; Mortensen, J. J.; Olsen, T.; Thygesen, K. S. The Computational 2D Materials Database: High-Throughput Modeling and Discovery of Atomically Thin Crystals. *2D Mater* **2018**, *5*, 042002.
(38) Richter, K. W.; Ipser, H. Transition Metal- Chalcogen Systems XI: The Platinum- Selenium Phase Diagram. *J. Phase Equilib.* **1994**, *15*, 165−170.
(39) Bannister, F. A. Determination of Minerals in Platinum Concentrates from the Transvaal by X-ray Methods. *Mineral. Mag. J. Mineral. Soc.* **1932**, *23*, 188−206.
(40) Huang, J.; Dong, N.; McEvoy, N.; Wang, L.; Coileain, C.; Wang, H.; Cullen, C. P.; Chen, C.; Zhang, S.; Zhang, L.; Wang, J. Surface-State Assisted Carrier Recombination and Optical Non-linearities in Bulk to 2D Nonlayered PtS. *ACS Nano* **2019**, *13*, 13390−13402.
(41) O'Brien, M.; McEvoy, N.; Motta, C.; Zheng, J.-Y.; Berner, N. C.; Kotakoski, J.; Elibol, K.; Pennycook, T. J.; Meyer, J. C.; Yim, C.; Abid, M.; Hallam, T.; Donegan, J. F.; Sanvito, S.; Duesberg, G. S. Raman Characterization of Platinum Diselenide Thin Films. *2D Mater.* **2016**, *3*, 021004.
(42) Gulo, D. P.; Yeh, H.; Chang, W.-H.; Liu, H.-L. Temperature-Dependent Optical and Vibrational Properties of $PtSe_2$ Thin Films. *Sci. Rep.* **2020**, *10*, 19003.
(43) Cho, S.; Kim, S.; Kim, J. H.; Zhao, J.; Seok, J.; Keum, D. H.; Baik, J.; Choe, D.-H.; Chang, K. J.; Suenaga, K.; Kim, S. W.; Lee, Y. H.; Yang, H. Phase Patterning for Ohmic Homojunction Contact in $MoTe_2$. *Science* **2015**, *349*, 625−628.
(44) Kirklin, S.; Saal, J. E.; Meredig, B.; Thompson, A.; Doak, J. W.; Aykol, M.; Rühl, S.; Wolverton, C. The Open Quantum Materials Database (OQMD): Assessing the Accuracy of DFT Formation Energies. *npj Comp. Mater.* **2015**, *1*, 15010.

https://doi.org/10.1021/acs.chemmater.1c02163
Chem. Mater. 2021, 33, 8018−8027